CRYSTAL GROWTH & DESIGN

pubs.acs.org/crystal

Article

Synthesis of High-Quality Monolayer MoS_2 via a CVD Upstream Deposition Strategy for Charge Capture and Collection

Tao Wang, Jiangtao Guo, Yong Zhang, Wen Yang, Xiaobo Feng, Jing Li, and Peizhi Yang*

Cite This: *Cryst. Growth Des.* 2024, 24, 2755−2763

Read Online

ACCESS | Metrics & More | Article Recommendations

ABSTRACT: Molybdenum disulfide (MoS_2) bears great potential in high-performance functional devices because of its tunable band structure, large surface area, and high charge carrier mobility. However, fabricating high-quality monolayer MoS_2 via chemical vapor deposition still faces challenges. Here, an upstream deposition strategy is reported to obtain a high-quality monolayer MoS_2 with high nucleation density and uniformity. Compared with the conventional downstream deposition method, the upstream deposition method presents excellent morphological characteristics. More importantly, MoS_2 prepared by the upstream deposition method shows a stronger charge capture ability at the liquid−solid interface.

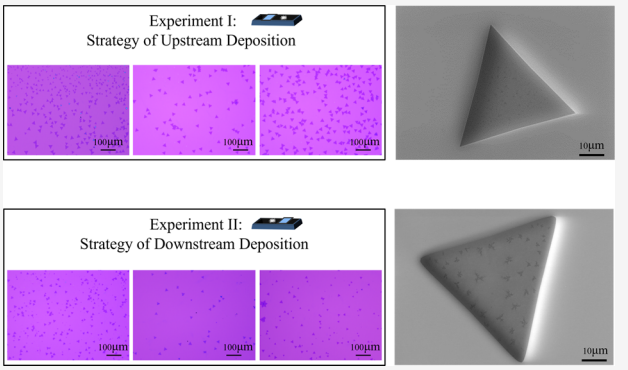

1. INTRODUCTION

Transition-metal dichalcogenides (TMDs) have attracted widespread attention because of their large surface area, excellent carrier mobility, and tunable energy band structure.[1−5] Molybdenum disulfide (MoS_2), as a representative material of TMDs, has a thickness-dependent bandgap.[6−8] The MoS_2 band structure undergoes an indirect-to-direct bandgap transition when the number of layers is reduced from bulk to a single layer.[9,10] Monolayer MoS_2 serves as an excellent platform for developing novel atomic thin electronic, optoelectronic, and photonic devices with high performance, such as field effect transistor, photodetectors, solar cells, light-emitting diodes, optical modulators, etc.[11]

Compared with traditional electrode materials and other two-dimensional materials, TMDs also show superior potential for applications in energy storage.[12−14] They possess several advantages, including a large electrochemically active surface area, tunable high surface area, abundant coordination sites, as well as both "Faradaic" and "non-Faradaic" electrochemical behaviors.[15] These characteristics make TMDs promising materials for high-performance energy harvesting devices,[16] capacitive charging devices,[17] and capacitive mechanical sensors.[18] Traditional MoS_2 energy conversion devices, such as hydrovoltaic nanogenerators and friction-based nanogenerators, have demonstrated great potential for the application of two-dimensional materials. Unfortunately, the utilization of MoS_2 fabricated through chemical vapor deposition (CVD) processes typically involves transfer steps, which can result in sample contamination or complex device assembly procedures. Therefore, Aji et al.[19] and Kumar et al.[20] suggested the gas-phase deposition technique to fabricate large-area MoS_2 films and utilized them as efficient energy harvesters in nanogenerators. These devices exhibit substantial output voltage generation, demonstrating strong capabilities in energy harvesting and power generation. Also, the conception of a direct current mode liquid-based triboelectric nanogenerator (TENG) was initially proposed by Dong et al.[21] Subsequently, continuous optimization and development were carried out,[22] demonstrating the potential applications of TENG as a probe for liquid−solid interfacial charge phenomena.

To fabricate high-quality MoS_2, up to now, one of the biggest challenges is how to obtain a high nucleation density (HND) on the substrate in order to grow large-scale uniform monolayer MoS_2. The research and applications of MoS_2 rely largely on efficient methods to obtain monolayers either from their bulk crystals or through direct thin-film growth.[23,24] Among these methods, the CVD method has been considered the most promising method in industrial production applications, due to its low cost, high quality, and large area.[25,26] However, the uneven gas flow inside the furnace results in the nonuniformity of the deposited flake in conventional CVD methods. In addition, the concentration

Received: November 16, 2023
Revised: March 5, 2024
Accepted: March 8, 2024
Published: March 22, 2024

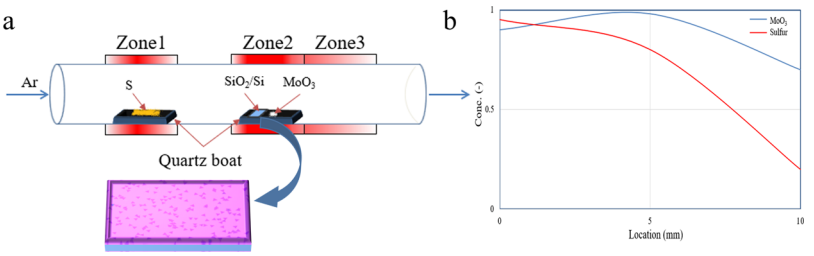

Figure 1. (a) Schematic diagram of the CVD system for MoS_2 synthesis. (b) Concentration distribution profiles of the precursors near the quartz boat.

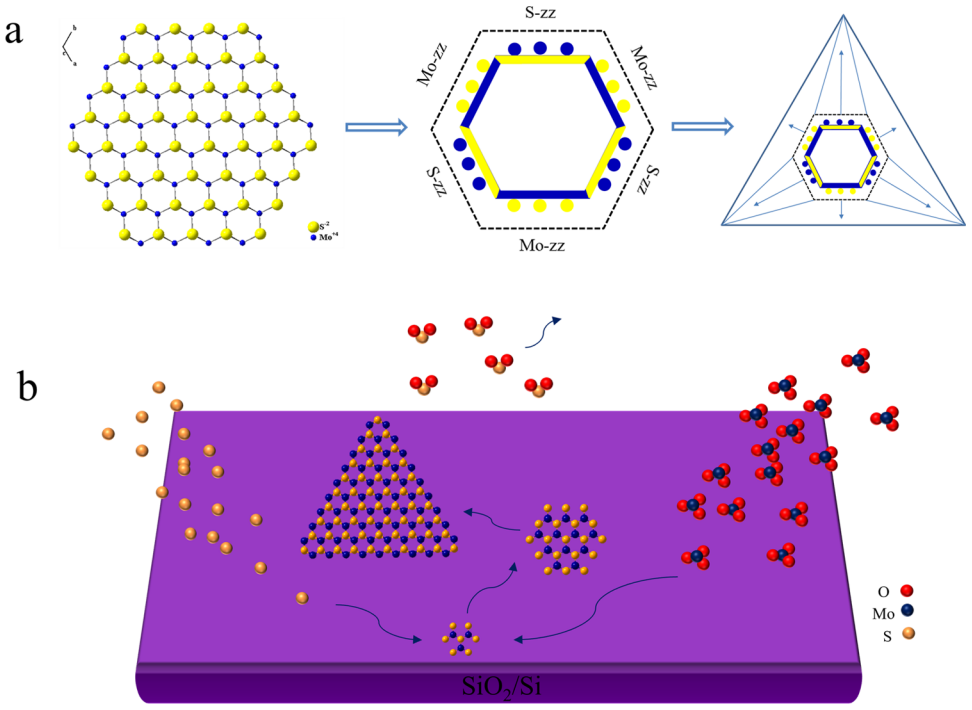

Figure 2. (a) Growth mechanism diagram of morphology within MoS_2. (b) Nucleation growth process on the substrate.

of precursors is also one of the key factors in affecting the deposition of high-quality MoS_2.[27,28] The CVD deposited TMD monolayers often exhibit inhomogeneity in optical and electrical properties.[29,30]

To solve this problem, Feng et al.[31] developed a liquid-precursor CVD (LCVD) method and obtained uniformly dispersed monolayer MoS_2. They used a solution that contains sulfur thiol (dodecyl mercaptan, $C_{12}H_{25}SH$) as the sulfur source and introduced it into the tube furnace in the form of bubbling. The precursor concentration can be precisely controlled, and sulfur sources can be steadily supplied during the reaction to participate in the deposition process, thus ensuring a uniform distribution of monolayer MoS_2 on the substrate. Similarly, Guo et al.[32] designed a vertically aligned CVD (VA-CVD) configuration assisted by a perforated carbon nanotube (p-CNT) film. VA-CVD configuration can avoid the precursor concentration gradient existing in the common horizontal CVD configuration. The p-CNT film plays a role in precursor supply and gas concentration regulation, contributing to achieving uniform distribution of gas flow rate and precursor concentration near the substrate, which improves the uniform wafer-scale growth of monolayer MoS_2.

Here, a new strategy, upstream deposition, is presented to achieve the rapid and uniform growth of high-quality monolayer MoS_2 on SiO_2/Si substrates. Specifically, this approach similarly involves the use of MoO_3 and sulfur powder as precursors, but these are placed in different temperature zones of the CVD furnace to enable efficient precursor decomposition and reaction. By positioning the substrate in the upstream area, in contrast to the commonly used lower stream area relative to the molybdenum source, we achieve denser nucleation sites and excellent uniformity of the MoS_2 flake. The impact of different morphological features on the material's electrical properties was investigated by employing a TENG as a probe for charge transfer, where open-circuit voltage (V_{oc}), transferred charge, and short-circuit current (I_{sc}) of MoS_2 were measured. Overall, this work provides a route for the scalable and reproducible synthesis of high-quality MoS_2 flakes for various applications, while also enhancing the potential of MoS_2 in the field of TENG.

2. EXPERIMENTAL DETAILS

2.1. Synthesis of MoS_2. In this work, the CVD method was used to prepare monolayer MoS_2 flakes. Before growth, S (99.5%, 300 mg) and MoO_3 (99.95%, 5 mg) powder, used as precursors, were placed in two quartz boats (1.5 cm × 10 cm), respectively. S powder was placed upstream of the tube furnace (zone 1), 20 cm away from the substrate, and MoO_3 powder was placed downstream of the substrate (both in zone 2). Figure 1 schematically shows the arrangement. As

https://doi.org/10.1021/acs.cgd.3c01369
Cryst. Growth Des. 2024, 24, 2755−2763

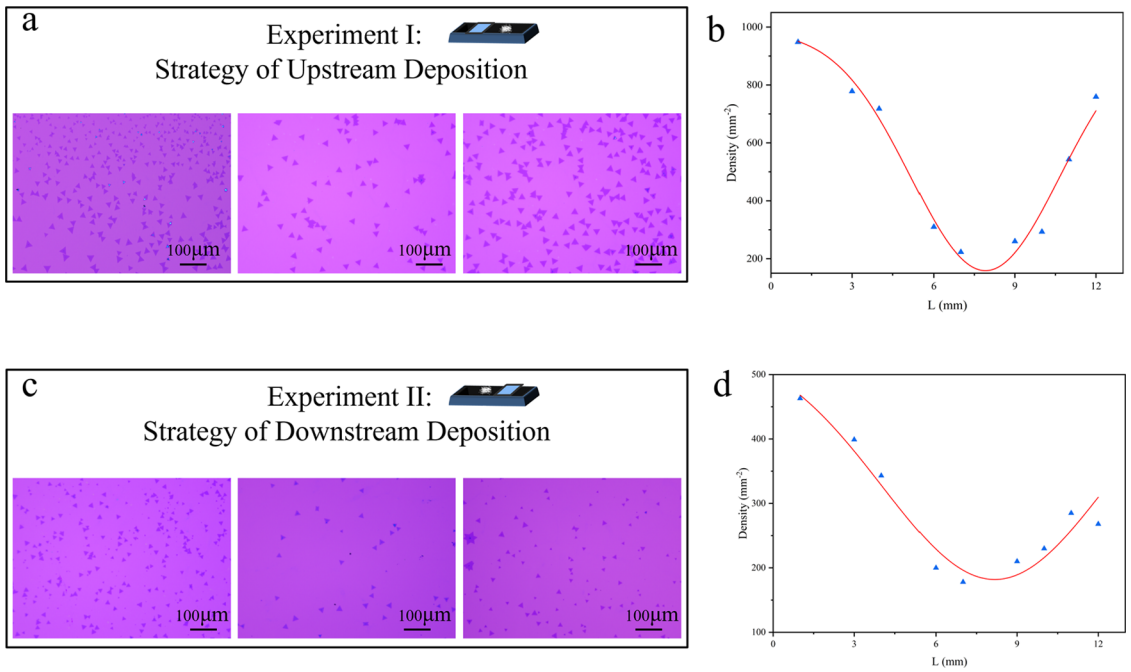

Figure 3. (a) OM images of samples from the upstream deposition experiment and (b) corresponding results of the crystal density. (c) OM images of samples from the downstream deposition experiment and (d) corresponding results of the crystal density.

shown in Figure 1a, the CVD tube furnace can be roughly divided into a low-temperature zone (zone 1) and two high-temperature zones (zones 2 and 3), and the monolayer MoS_2 is deposited in zone 2. Specifically, a cleaned SiO_2/Si (1.0 cm × 1.2 cm) substrate covered the upper stream side of the quartz boat containing MoO_3 powder. Furnace was flushed for 20 min with 600 sccm of Ar gas at room temperature. Then, after the temperatures of zone 1 and zone 2 reached their respective target values (290 °C for S powder, 890 °C for MoO_3), under atmospheric pressure, 20 sccm of argon flow was introduced as the carrier gas, and a stable deposition time of 10 min was needed. Finally, the samples were naturally cooled to room temperature in a 300 sccm argon flow.

2.2. Fabrication MoS_2-Based TENG. The synthetic $MoS_2/SiO_2/Si$ is fixed on an acrylic plate (20 × 30 × 0.1 mm), and the polytetrafluoroethylene (PTFE) film is seamlessly connected to it. A conductive silver cloth is attached to the lower end of the MoS_2 flake to form an electrical connection, and a Cu electrode is attached to the top of the PTFE film to form an electrical connection.

2.3. Characterizations and Measurements. Optical microscopy (OM, Nikon LV100), scanning electron microscopy (SEM, ZEISS Sigma 300), atomic force microscopy (AFM, Bruker Dimension Icon), X-ray photoelectron spectroscopy analysis (XPS, ESCALAB 250Xi), and Raman spectroscopy (iHR320, Horiba with 532 nm laser) were used to characterize the synthesized MoS_2 samples. ImageJ was used to analyze the crystal nucleation density at various positions on the substrate, using an effective edge length defined as $\sqrt{\frac{4A}{\sqrt{3}}}$ (where A is the area of the crystal). A static collection system (Keithley 6514) was used to measure the transferred charge, short-circuit current, and open-circuit voltage.

3. RESULTS AND DISCUSSION

3.1. Process and Principles of the Upstream Deposition Strategy. As shown in Figure 1a, because the thermal insulation of a portion of the tube between zones 1 and 2 is removed and thus the tube in this section is exposed to air at close to room temperature, the temperature difference between zones 1 and 2 in the upstream of the tube furnace is greater than that in the downstream position in zone 3. According to the ideal gas equation of state in thermodynamics, $PV = nkT$ (P stands for pressure, V stands for volume of gas, n stands for amount of substance, k stands for gas constant, and T stands for temperature), the pressure is directly proportional to temperature, which results in a higher concentration of precursor vapor in the upstream. The concentration distributions are depicted in Figure 1b.[33] Therefore, we adopted the strategy of depositing monolayer MoS_2 by placing the substrate upstream from the Mo source.

3.2. Growth Mechanism of Monolayer MoS_2. In order to clearly explain the likelihood of growing high-quality single-layer MoS_2 flakes in the upstream region, a schematic diagram of the potential growth mechanism is shown in Figure 2a.[33,34] The morphology of MoS_2 is mainly related to the growth rates of the S-zz and Mo-zz edges. The upstream region has a high Mo vapor concentration (the overall ratio S: Mo < 2:1), and the exposed unsaturated S atoms more easily bond with free Mo atoms due to excess Mo source.[35] Therefore, the S-zz edge has a faster growth rate, while the Mo-zz edge has a relatively slow growth rate. As the reaction continues, the crystal eventually grows into inverted triangles. In general, the utilization of upstream deposition enables the precursor to undergo reactions in a reduced distance and time, thereby minimizing the diffusion distance of the deposited material on the substrate. This approach effectively reduces thickness gradients and compositional variations, resulting in improved uniformity and quality of the sample. Moreover, the condition of a high concentration Mo precursor supply promotes the generation of a greater quantity of nucleation sites, leading to a substantial improvement in the nucleation density (Figure 2b).

3.3. Influence of Deposition Strategies on MoS_2. We conducted two experiments to validate this hypothesis, namely, the upstream and downstream deposition strategies. The results of the deposited samples are shown in Figure 3. Figure 3a displays the OM images of MoS_2, by using the upstream deposition strategy to synthesize the samples. Observations were made at different positions on the substrate, and

https://doi.org/10.1021/acs.cgd.3c01369
Cryst. Growth Des. 2024, 24, 2755−2763

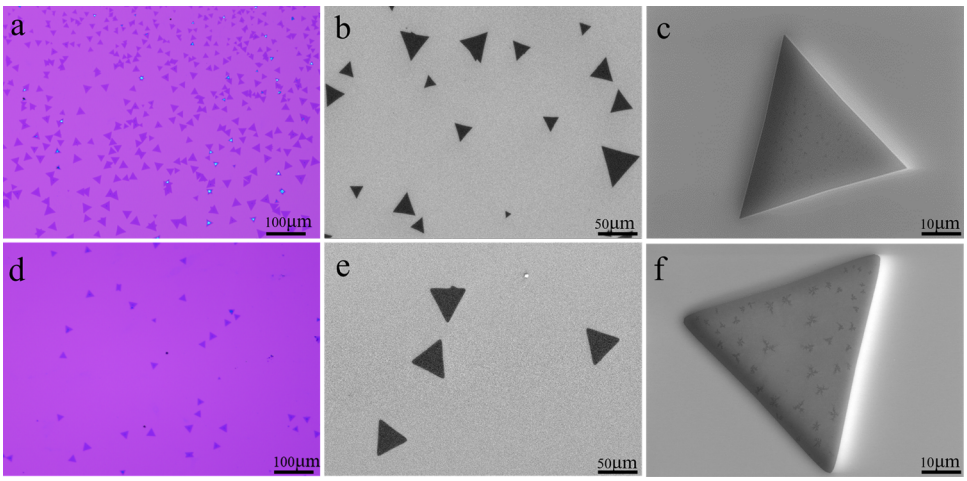

Figure 4. (a) OM image of the CVD deposited MoS_2 by upstream deposition. The SEM images: (b) low magnification and (c) high magnification. (d) OM image of the MoS_2 by downstream deposition. The SEM images: (e) low magnification and (f) high magnification.

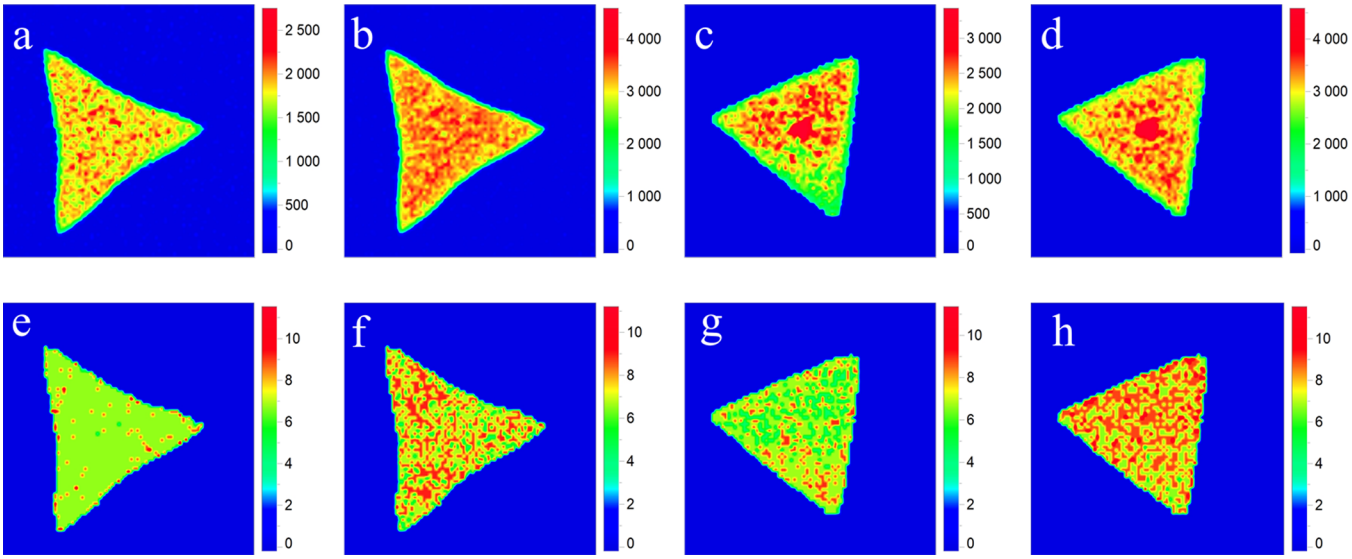

Figure 5. Raman mapping of monolayer MoS_2 (50 μm × 50 μm). The upstream deposition: (a, b) intensity maps of the E^1_{2g} mode and A_{1g} mode, respectively. The downstream deposition: (c, d) intensity maps of the E^1_{2g} mode and A_{1g} mode, respectively. The upstream deposition: (e, f) fwhm maps of the E^1_{2g} mode and A_{1g} mode, respectively. The downstream deposition: (g, h) fwhm maps of the E^1_{2g} mode and A_{1g} mode, respectively.

subsequently, the crystal nucleation density was calculated, as illustrated in Figure 3b. The growth pattern of MoS_2 on the substrate followed a U-shaped trend, with a higher nucleation density observed near the substrate's edges and a relatively lower distribution in the central region. In Figure 3c, we present the similar OM images of a sample that used the downstream deposition strategy. The growth pattern observed in the second sample was consistent with that in the first one. However, the overall crystal nucleation density in the downstream sample was significantly lower, as depicted in Figure 3d. Therefore, we demonstrated that the upstream deposition strategy can indeed significantly enhance the crystal nucleation density of MoS_2 on the substrate.

In order to further compare the two deposition methods, two MoS_2 samples deposited upstream and downstream were prepared and characterized by OM and SEM, as shown in Figure 4. Figure 4a presents a typical OM image of MoS_2 deposited on the upstream substrate. High-density MoS_2 domains exhibit an equilateral triangular shape with an edge size of approximately 43.5 μm. The uniform optical contrast suggests that the thickness of the MoS_2 deposited is uniform. To further evaluate the morphology of the individual monolayer MoS_2 domains, we conducted SEM analysis. The results, as shown in Figure 4b,c, reveal a flat and smooth surface of monolayer MoS_2 with sharp edges. In contrast, when the substrate was placed downstream, similar equilateral triangular-shaped domains were observed, as shown in Figure 4d, but with a much lower density. OM images displayed uniform optical contrast with a reduced lateral dimension of approximately 39.7 μm. It is worth noting that the lower density of the crystal domains is the direct consequence of the less nucleation sites formed on the substrate. The corresponding SEM images (Figure 4e,f) also revealed distinct flower-like patterns on the sample surface, and the edges appeared slightly rounded. Therefore, samples prepared by upstream deposition exhibit a higher crystalline quality.

In order to determine the uniformity of monolayer MoS_2 synthesized using both strategies in terms of their material properties, high spatial resolution Raman mappings were conducted on the samples, as shown in Figure 4, by

https://doi.org/10.1021/acs.cgd.3c01369
Cryst. Growth Des. 2024, 24, 2755−2763

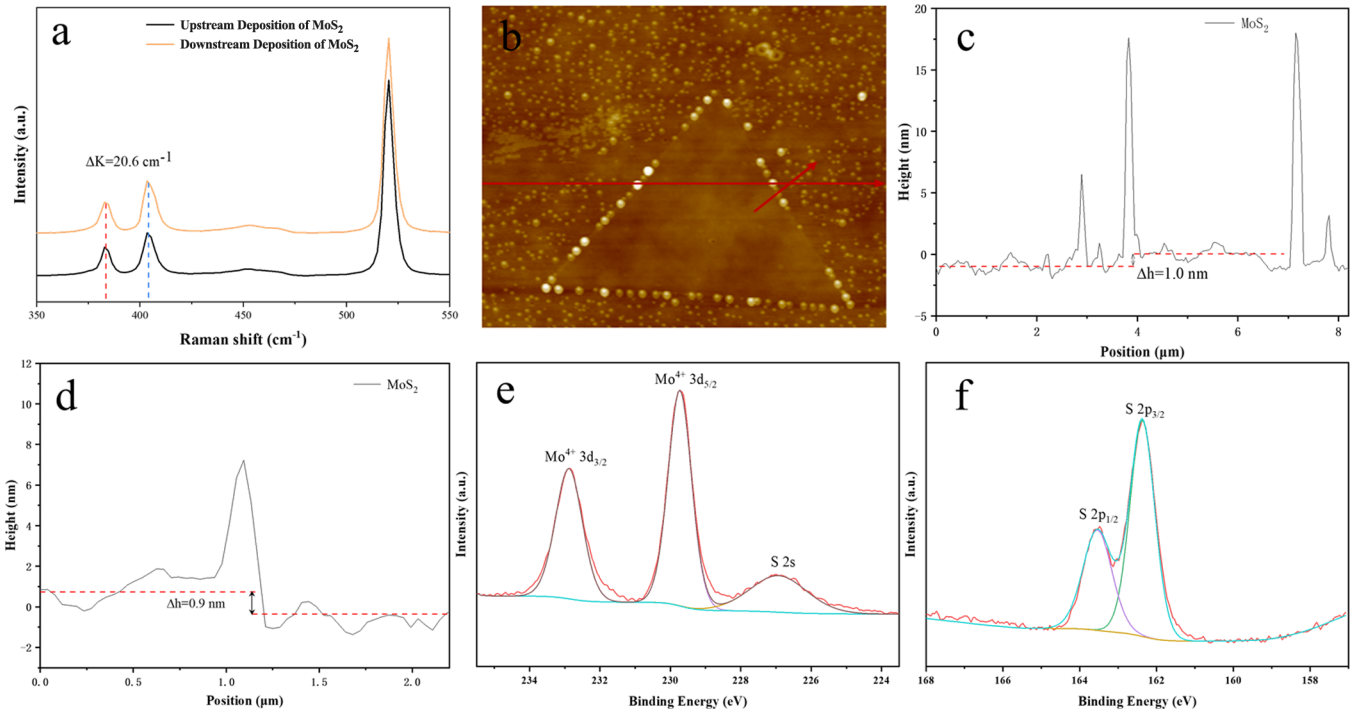

Figure 6. (a) Raman spectrum of upstream-grown monolayer MoS_2. (b) AFM image of the MoS_2 flake. The height profiles (c) and (d) are along the two red lines in (b). (e) XPS spectra of Mo 3d and (f) S 2p.

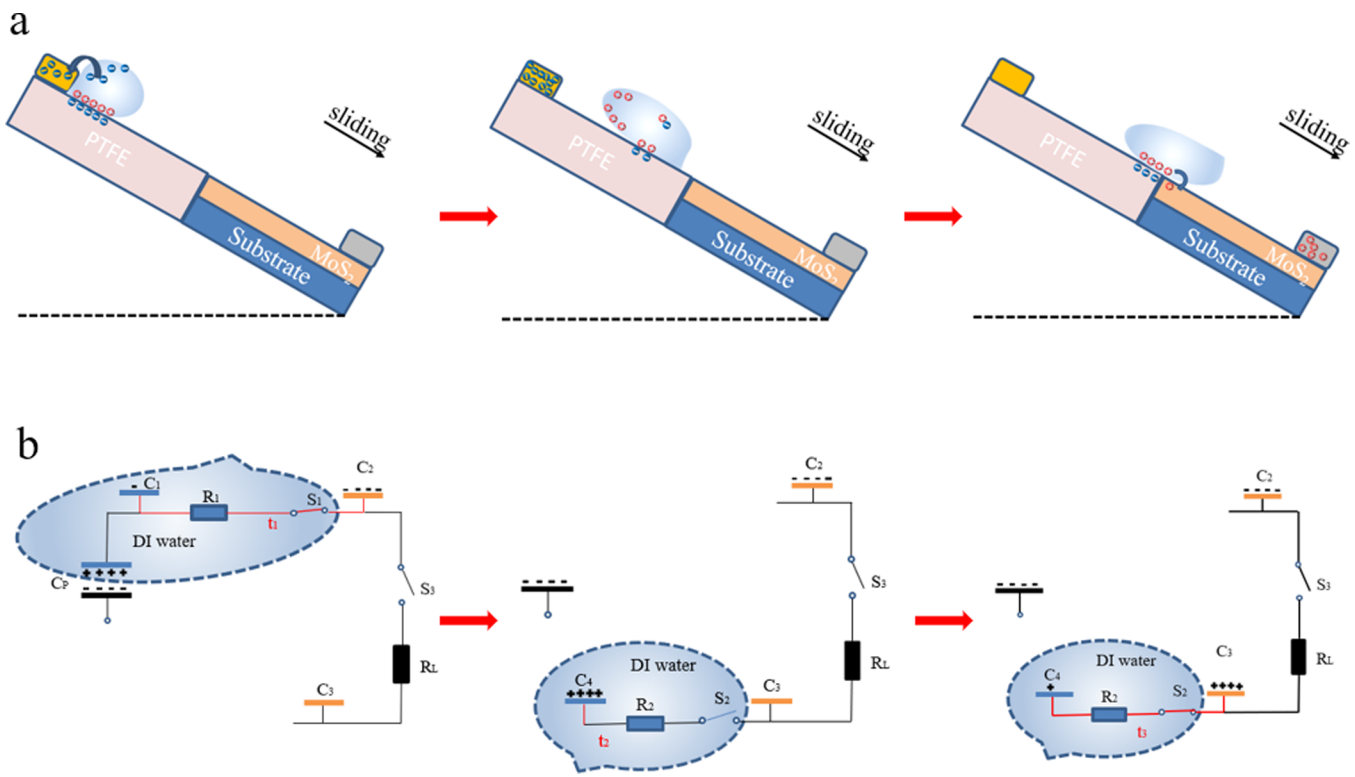

Figure 7. Working mechanism (a) and equivalent circuit (b) of the MoS_2-based TENG. Step I, charge transfer from the water to the top electrode; step II, the hydrophobicity of PTFE and the effect of gravity enable charge separation; and step III, MoS_2 collects and transfers positive charges.

characterizing the peak intensities and peak widths of two characteristic Raman peaks E^1_{2g} and A_{1g}, as shown in Figure 5. The E^1_{2g} mode corresponds to the in-plane vibration of Mo and S atoms in the opposite direction, while A_{1g} is the out-of-plane vibration mode of S atoms.[36] In Figure 5a,b, it can be observed that the sample synthesized using the upstream deposition method exhibits more uniform intensity distributions of the E^1_{2g} and A_{1g} modes compared with the downstream deposition (Figure 5c,d). The comparison indicates superior uniformity in the upstream-deposited

https://doi.org/10.1021/acs.cgd.3c01369
Cryst. Growth Des. 2024, 24, 2755−2763

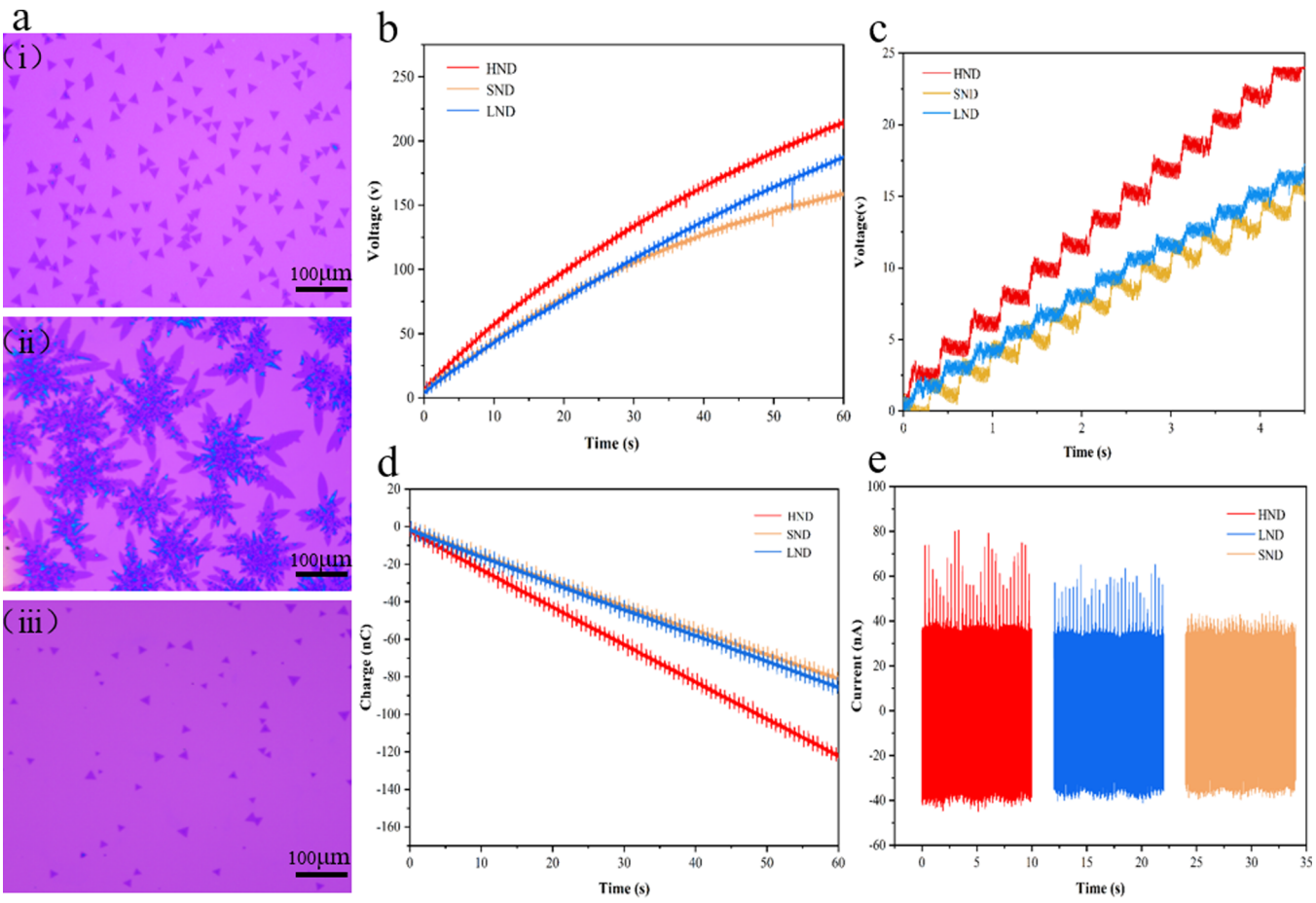

Figure 8. (a) Optical microscope images of different morphologies: (i) HND, (ii) SND, and (iii) LND. Electrical performance testing: (b,c) V_{oc}, (d) transferred charge, and (e) I_{sc}.

sample. Furthermore, as illustrated in Figure 5e,f, the upstream-deposited sample displays more uniformly distributed and narrower peak widths for the E^1_{2g} and A_{1g} modes, indicating excellent crystalline quality, whereas the overall peak widths increase and uniformity decrease in the downstream-deposited sample (Figure 5g,h). Based on these results, the main conclusion that can be drawn is that the samples which were prepared using the upstream deposition strategy contribute to superior uniformity and quality.

3.4. Thickness and Phase Analysis of Monolayer MoS_2. The layer number of the sample obtained from upstream deposition was confirmed by Raman spectroscopy, as shown in Figure 6a. The E^1_{2g} mode and A_{1g} mode were found at 383.1 and 403.7 cm^{-1}, respectively. The frequency difference can be obtained by subtracting E^1_{2g} from A_{1g}, which is 20.6 cm^{-1}. Meanwhile, the value of frequency difference indicates that the thickness of the upstream sample corresponds to that of monolayer MoS_2.[37,38] The layer number of the sample was further evaluated using AFM analysis, and the characterization result is shown in Figure 6b. The AFM image of MoS_2 shown in Figure 6b infers that the morphology is consistent with the SEM image in Figure 4c. Figure 6c,d shows the height profiles of the sample, corresponding to the two line scans indicated in Figure 6b, respectively. The thickness of 0.9−1.0 nm was demonstrated through the height profile scanning, which is consistent with the expected thickness of a monolayer MoS_2.[39]

To analyze the binding energy of Mo and S atoms in the MoS_2 flake deposited at the upstream position, XPS was performed. The binding energy was calibrated with the C 1s peak (284.6 eV) as a reference. The Mo 3d spectrum (Figure 6e) displays two characteristic peaks at 232.7 and 229.6 eV, corresponding to the Mo $3d_{3/2}$ and $3d_{5/2}$ orbitals, respectively. Figure 6f shows the characteristic peaks at 162.3 and 163.5 eV originate from the S $2p_{2/3}$ and $2p_{1/2}$ orbitals. The obtained binding energies are the same as previously reported values for MoS_2.[40,41] The expected charge states of Mo^{4+} and S^{2-} in MoS_2 have been proved, and no additional peak has been observed. These results demonstrate the high purity of the MoS_2 flake and confirm that MoO_3 is fully sulfurized to form the hexagonal MoS_2 crystalline structure.

3.5. Electrical Performance Testing of MoS_2-Based TENG. We utilized the TENG as a probe for the charge transfer. Meanwhile, the charge transfer characteristics at the liquid−solid interface were utilized to investigate the electrical performance and influencing factors of the monolayer MoS_2, which achieved the in situ construction of a TENG based on a similar direct water-droplet mode without the need for complex processes. The TENG probe structure consists of a top copper electrode, a PTFE friction layer, and a bottom electrode MoS_2/Ag. To provide a deeper understanding of its working principle, we present the process of charge generation, transfer, and accumulation during the droplet sliding process (Figure 7a), along with the corresponding circuit structure at each stage (Figure 7b).

https://doi.org/10.1021/acs.cgd.3c01369
Cryst. Growth Des. 2024, 24, 2755−2763

The working principle of the MoS_2-based TENG is as follows: By using deionized water as the charge carrier, the falling droplets contact the liquid−solid interfaces of both the Cu and Ag electrodes, forming a direct current circuit of the TENG and generating charge accumulation. Upon contacting the top electrode, the droplets transfer negative charges to the electrode due to a spontaneous electric field, facilitating the collection of negative charges. As the droplets continue to slide on the PTFE surface for a certain distance, the system has no output due to the electrostatic shielding effect of the electric double layer. However, when the edge of droplet meets the surface of MoS_2, a conductive pathway is formed at the water/MoS_2 interface. Due to the potential difference in the system, positive charges are collected by MoS_2 under the driving force of the electric field.

Subsequently, we investigated charge transfer at the liquid−solid interface of the probe during its operation. With the number of droplets increased, it could be observed that the continuous transfer and storage of charges between the top negative electrode and the bottom MoS_2 layer acting as the positive electrode resulted in an increase in the transferred charge amount and V_{oc}, following a pattern similar to the direct current mode. It is worth noting that the monolayer MoS_2 itself possesses excellent interface charge trapping capability, indicating a similarity between the charge transfer process at the liquid−solid interface and the conventional electrode-based charge collection.

To demonstrate the differences in the electrical performance of MoS_2 devices based on CVD processes with different parameters, we selected three representative samples: high nucleation density with uniform dispersion defined as high nucleation density (HND), high nucleation density with stacked snowflake-like morphology defined as stacked nucleation density (SND), and low nucleation density with uniform dispersion defined as low nucleation density (LND), as shown in Figure 8a.

By conducting V_{oc} accumulation mode tests, we observed that the HND sample exhibited the fastest voltage accumulation rate, the maximum voltage is 217.8 V, while the LND sample had a slightly faster accumulation rate compared to the SND sample, as shown in Figure 8b. Furthermore, by reducing the time for voltage accumulation mode testing to 4.5 s, we observed a steady stepwise increase in voltage, showing a linear growth pattern with growth rates of 5.5, 3.7, and 3.5 V/s, respectively, as shown in Figure 8c.

Figure 8d,e represents the charge accumulation and I_{sc} generated by the MoS_2-based TENG, respectively. The I_{sc} for HND, LND, and SND were measured as 80.96, 64.80, and 44.21 nA, while the corresponding transferred charges were 124.41, 85.95, and 81.53 nC. The trends in I_{sc} and transferred charge for all three devices were consistent with the V_{oc}. The results indicate that the HND sample exhibits superior charge capture performance at the water/MoS_2 interface, which is attributed to its well-dispersed and high-density nucleation distribution. This could potentially account for its higher output signal compared to the SND and LND samples. Therefore, we believe that MoS_2 with good dispersion and high-density crystal domains contributes to capturing and storing more charge at the MoS_2/SiO_2/P-type Si interface and on the surface of MoS_2 in the device.

4. CONCLUSIONS

In conclusion, we fabricated high-quality monolayer MoS_2 flakes by using the upstream deposition strategy. Through structural and property characterization and analysis, we have found that the upstream deposition strategy exhibits certain advantages compared with the downstream deposition by achieving HND and uniformity of individual crystal domains. Meanwhile, we employed the friction-based nanogenerator as a charge transfer probe to evaluate the electrical performance of three different morphologies: HND, SND, and LND. Notably, the HND morphology demonstrated a higher open-circuit voltage (V_{oc}), charge accumulation, and short-circuit current (I_{sc}). This indicates that the sample morphology obtained through upstream deposition possesses superior energy harvesting and power generation capabilities. Additionally, the one-step integration of such devices eliminates the need for substrate transfer, which simplifies the device fabrication process. This streamlined approach contributes to the broader application of MoS_2 in various functional devices.

AUTHOR INFORMATION

Corresponding Author

Peizhi Yang − *Key Laboratory of Advanced Technique and Preparation for Renewable Energy Materials, Ministry of Education, Yunnan Normal University, Kunming 650500, P. R. China; Southwest United Graduate School, Kunming 650092, China*; Email: pzhyang@hotmail.com

Authors

Tao Wang − *Key Laboratory of Advanced Technique and Preparation for Renewable Energy Materials, Ministry of Education, Yunnan Normal University, Kunming 650500, P. R. China*; orcid.org/0009-0006-3587-3874

Jiangtao Guo − *Key Laboratory of Advanced Technique and Preparation for Renewable Energy Materials, Ministry of Education, Yunnan Normal University, Kunming 650500, P. R. China*

Yong Zhang − *Department of Electrical and Computer Engineering and Center for Optoelectronics, University of North Carolina at Charlotte, Charlotte, North Carolina 28223, United States*; orcid.org/0000-0003-4781-1583

Wen Yang − *Key Laboratory of Advanced Technique and Preparation for Renewable Energy Materials, Ministry of Education, Yunnan Normal University, Kunming 650500, P. R. China*

Xiaobo Feng − *Key Laboratory of Advanced Technique and Preparation for Renewable Energy Materials, Ministry of Education, Yunnan Normal University, Kunming 650500, P. R. China*

Jing Li − *Key Laboratory of Advanced Technique and Preparation for Renewable Energy Materials, Ministry of Education, Yunnan Normal University, Kunming 650500, P. R. China*

Complete contact information is available at: https://pubs.acs.org/10.1021/acs.cgd.3c01369

Author Contributions

P.Y. designed and directed the study. T.W. performed the preparation of MoS_2 and MoS_2-based TENG designs with the help of J.G. and X.F. T.W. and J.L. wrote the manuscript. W.Y. provided help with the growth of flakes. Y.Z. assisted with test characterizations and article revision. P.Y. provided financial

https://doi.org/10.1021/acs.cgd.3c01369
Cryst. Growth Des. 2024, 24, 2755−2763

support for the experimental work. All authors have approved the final version of the manuscript.

Notes

The authors declare no competing financial interest.

■ ACKNOWLEDGMENTS

This work was supported by the National Natural Science Foundation of China (U1802257 and 12264057), the Key Applied Basic Research Program of Yunnan Province (202201AS070023), Yunnan Revitalization Talent Support Program, and the Spring City Plan: The High-level Talent Promotion and Training Project of Kunming (2022SCP005).

■ REFERENCES

(1) Cheng, Z.; Cao, R.; Wei, K.; Yao, Y.; Liu, X.; Kang, J.; Dong, J.; Shi, Z.; Zhang, H.; Zhang, X. 2D Materials Enabled Next-Generation Integrated Optoelectronics: From Fabrication to Applications. *Adv. Sci.* **2021**, *8*, No. 2003834.

(2) Zhao, Y.; Huang, J.; Chen, J.; Liu, Y.; Zhai, T. Chemical-Vapor-Deposition-Grown 2D Transition Metal Dichalcogenides: A Generalist Model for Engineering Electrocatalytic Hydrogen Evolution. *Nano Res.* **2023**, *16*, 101−116.

(3) Wang, W.; Zeng, X.; Warner, J.; Gou, Z.; Hu, Y.; Zeng, Y.; Lu, J.; Jin, W.; Wang, S.; Lu, J. Photoresponse-Bias Modulation of a High-Performance MoS_2 Photodetector with A Unique Vertically Stacked 2H-MoS_2/1T@ 2H-MoS_2 Structure. *ACS Appl. Mater. Interfaces* **2020**, *12*, 33325−33335.

(4) Rao, T.; Wang, H.; Zeng, Y.; Gou, Z.; Liao, W. Phase Transitions and Water Splitting Applications of 2D Transition Metal Dichalcogenides and Metal Phosphorous Trichalcogenides. *Adv. Sci.* **2021**, *8*, No. 202002284.

(5) Huang, H.; Zha, J.; Li, S.; Tan, C. Two-Dimensional Alloyed Transition Metal Dichalcogenide Nanosheets: Synthesis and Applications. *Chin. Chem. Lett.* **2022**, *33*, 163−176.

(6) Mak, K.; Lee, C.; Hone, J.; Shan, J.; Heinz, T. Atomically Thin MoS_2: A New Direct-Gap Semiconductor. *Phys. Re. Lett.* **2010**, *105*, 13680.

(7) Splendiani, A.; Sun, L.; Zhang, Y.; Li, T.; Kim, J.; Chim, C. Y.; Galli, G.; Wang, F. Emerging Photoluminescence in Monolayer MoS_2. *Nano Lett.* **2010**, *10*, 1271−1275.

(8) Li, H.; Ling, J.; Lin, J.; Lu, X.; Xu, W. Interface Engineering in Two-Dimensional Heterostructures Towards Novel Emitters. *J. Semicond.* **2023**, *4*, No. 011001.

(9) Xu, H.; Zhu, J.; Ma, Q.; Ma, J.; Bai, H.; Chen, L.; Mu, S. Two-Dimensional MoS_2: Structural Properties, Synthesis Methods, and Regulation Strategies toward Oxygen Reduction. *Micromachines* **2021**, *12*, 240.

(10) Ren, X.; Pang, L.; Zhang, Y.; Ren, X.; Fan, H.; Liu, S. One-Step Hydrothermal Synthesis of Monolayer MoS_2 Quantum Dots for Highly Efficient Electrocatalytic Hydrogen Evolution. *J. Mater. Chem. A* **2015**, *3*, 10693−10697.

(11) Huang, L.; Krasnok, A.; ALú, A.; Yu, Y.; Neshev, D.; Miroshnichenko, A. Enhanced Light−Matter Interaction in Two-Dimensional Transition Metal Dichalcogenides. *Rep. Prog. Phys.* **2022**, *85*, No. 046401.

(12) Dahiya, Y.; Hariram, M.; Kumar, M.; Jain, A.; Sarkar, D. Modified Transition Metal Chalcogenides for High Performance Supercapacitors: Current Trends and Emerging Opportunities. *Coordin. Chem. Rev.* **2022**, *451*, No. 214265.

(13) Bissett, M.; Worrall, S.; Kinloch, I.; Dryfe, R. Comparison of Two-Dimensional Transition Metal Dichalcogenides for Electrochemical Supercapacitors. *Electrochim. Acta* **2016**, *201*, 30−37.

(14) Lin, L.; Lei, W.; Zhang, S.; Liu, Y.; Wallace, G.; Chen, J. Two-Dimensional Transition Metal Dichalcogenides in Supercapacitors and Secondary Batteries. *Energy Storage Mater.* **2019**, *19*, 408−423.

(15) Pace, G.; Castillo, A. E. D.; Lamperti, A.; Lauciello, S.; Bonaccorso, F. 2D Materials-based Electrochemical Triboelectric Nanogenerator. *Adv. Mater.* **2023**, *35*, No. 2211037.

(16) Cai, H.; Gou, Y.; Gao, H.; Guo, W. Tribo-Piezoelectricity in Janus Transition Metal Dichalcogenide Bilayers: A First-Principles Study. *Nano Energy* **2019**, *56*, 33−39.

(17) Choudhary, N.; Li, C.; Chung, H.; Moore, J.; Thomas, J.; Jung, Y. High-Performance One-Body Core/Shell Nanowire Supercapacitor Enabled by Conformal Growth of Capacitive 2D WS_2 Layer. *ACS Nano* **2016**, *10*, 10726−10735.

(18) Kim, T.; Park, I.; Kang, S.; Kim, T.; Choi, S. Enhanced Triboelectric Nanogenerator Based on Tungsten Disulfide via Thiolated Ligand Conjugation. *ACS Appl. Mater. Interfaces* **2021**, *13*, 21299−21309.

(19) Aji, A.; Nishi, R.; Ago, H.; Ohno, Y. High Output Voltage Generation of Over 5 V From Liquid Motion on Single-Layer MoS_2. *Nano Energy* **2020**, *68*, No. 104370.

(20) Kumar, S.; Sharma, A.; Gupta, V.; Tomar, M. Development of Novel MoS_2 Hydrovoltaic Nanogenerators for Electricity Generation from Moving NaCl Droplet. *J. Alloy. Compo.* **2021**, *884*, No. 161058.

(21) Dong, J.; Xu, C. Y.; Zhu, L.; Zhao, X.; Zhou, H.; Liu, H. W.; Xu, G.; Wang, G.; Zhou, G.; Zeng, Q. A High Voltage Direct Current Droplet-Based Electricity Generator Inspired by Thunderbolts. *Nano Energy* **2021**, *90*, No. 106567.

(22) Luo, B.; Liu, T.; Cai, C.; Yuan, J.; Liu, Y.; Gao, C.; Meng, X.; Wang, J.; Zhang, S.; Chi, M. Triboelectric Charge-Separable Probes for Quantificationally Charge Investigating at the Liquid-Solid Interface. *Nano Energy* **2023**, *113*, No. 108532.

(23) Liu, L.; Li, T.; Ma, L.; Li, W.; Gao, S.; Sun, W.; Dong, R.; Zou, X.; Fan, D.; Shao, L.; Gu, C.; Dai, N.; Yu, Z.; Chen, X.; Tu, X.; Nie, Y.; Wang, P.; Wang, J. Uniform Nucleation and Epitaxy of Bilayer Molybdenum Disulfide on Sapphire. *Nature* **2022**, *605*, 69.

(24) Zhang, Y.; Wang, Z.; Feng, J. H.; Ming, S.; Qu, F.; Xia, Y.; He, M.; Hu, Z.; Wang, J. Synthesis and Electromagnetic Transport of Large-Area 2D WTe_2 Thin Film. *J. Semicond.* **2022**, *43*, No. 102002.

(25) Yu, Y.; Li, C.; Liu, Y.; Su, L.; Zhang, Y.; Cao, L. Controlled Scalable Synthesis of Uniform, High-Quality Monolayer and Few-Layer MoS_2 Films. *Sci. Rep.* **2013**, *3*, 1866.

(26) Huang, X.; Han, X.; Dai, Y.; Xu, X.; Yan, J.; Huang, M.; Ding, P.; Zhang, D.; Chen, H.; Laxmi, V. Recent Progress on Fabrication and Flat-Band Physics in 2D Transition Metal Dichalcogenides Moire Superlattices. *J. Semicond.* **2023**, *44*, No. 011901.

(27) Zhang, Y.; Yao, Y. Y.; Sengeku, M.; Yin, L.; Zhan, X.; Wang, F.; Wang, Z.; He, J. Recent Progress in CVD Growth of 2D Transition Metal Dichalcogenides and Related Heterostructures. *Adv. Mater.* **2019**, *3*, No. 1901694.

(28) Ye, Z.; Tan, C.; Huang, X.; Ouyang, Y.; Yang, L.; Wang, Z.; Dong, M. Emerging MoS_2 Wafer-Scale Technique for Integrated Circuits. *Nano-Micro Lett.* **2023**, *15*, 38.

(29) Lu, A.; Martins, L.; Shen, P.; Chen, Z.; Park, J.; Xue, M.; Han, J.; Mao, N.; Chiu, M.; Palacios, T. Unraveling the Correlation Between Raman and Photoluminescence in Monolayer MoS_2 Through Machine-Learning Models. *Adv. Mater.* **2022**, *34*, No. 2202911.

(30) Su, L.; Yu, Y.; Cao, L.; Zhang, Y. Correlative Spectroscopic Investigations of the Mechanisms of Inhomogeneity in CVD-Grown Monolayer WS_2. *Sci. China Mater.* **2023**, *66*, 3949.

(31) Feng, S.; Tan, J.; Zhao, S.; Zhang, S.; Khan, U.; Tang, L.; Zou, X.; Lin, J.; Cheng, H.; Liu, B. Synthesis of Ultrahigh-Quality Monolayer Molybdenum Disulfide Through in Situ Defect Healing with Thiol Molecules. *Small* **2020**, *16*, No. 2003357.

(32) Gou, J.; Peng, R.; Zhang, X.; Xin, Z.; Wang, E.; Wu, Y.; Li, C.; Fan, S.; Shi, R.; Liu, K. Perforated Carbon Nanotube Film Assisted Growth of Uniform Monolayer MoS_2. *Small* **2023**, *19*, No. 2300766.

(33) Rajan, A.; Warner, J.; Blankschtein, D.; Strano, M. Generalized Mechanistic Model for the Chemical Vapor Deposition of 2D Transition Metal Dichalcogenide Monolayers. *ACS Nano* **2016**, *10*, 4330−4344.

https://doi.org/10.1021/acs.cgd.3c01369
Cryst. Growth Des. 2024, 24, 2755−2763

(34) Wang, S.; Rong, Y.; Fan, Y.; Pacios, M.; Bhaskaran, H.; He, K.; Warner, J. Shape Evolution of Monolayer MoS_2 Crystals Grown by Chemical Vapor Deposition. *Chem. Mater.* **2014**, *26*, 6371−6379.
(35) Li, B.; Ju, Q.; Hong, W.; Cai, Q.; Lin, J.; Liu, W. Edge Defect-Assisted Synthesis of Chemical Vapor Deposited Bilayer Molybdenum Disulfide. *Ceram. Int.* **2021**, *47*, 30106−30112.
(36) Li, H.; Zhang, Q.; Yap, C.; Tay, B.; Edwin, T.; Olivier, A.; Baillargeat, D. From Bulk to Monolayer MoS_2: Evolution of Raman Scattering. *Adv. Funct. Mater.* **2012**, *22*, 1385−1390.
(37) Ling, X.; Lee, Y.; Lin, Y.; Fang, W.; Yu, L.; Dresselhaus, M.; Kong, J. Role of the Seeding Promoter in MoS_2 Growth by Chemical Vapor Deposition. *Nano Lett.* **2014**, *14*, 464−472.
(38) Najmaei, S.; Liu, Z.; Zhou, W.; Zou, X.; Shi, G.; Lei, S.; Yakobson, B.; Idrobo, J.; Ajayan, P.; Lou, J. Vapour Phase Growth and Grain Boundary Structure of Molybdenum Disulphide Atomic Layer. *Nat. Mater.* **2013**, *12*, 754−759.
(39) Chen, L.; Zang, L.; Chen, L.; Wu, J.; Jiang, C.; Song, J. Study on the Catalyst Effect of NaCl on MoS_2 Growth in a Chemical Vapor Deposition Process. *CrystEngComm* **2021**, *23*, 5337−5344.
(40) Higgins, E.; Mcadams, S.; Hopkinson, D.; Byrne, C.; Walton, A.; Lewis, D.; Dryfe, R. Room-Temperature Production of Nanocrystalline Molybdenum Disulfide (MoS_2) at the Liquid-Liquid Interface. *Chem. Mater.* **2019**, *31*, 5384−5391.
(41) Chen, F.; Su, W. The Effect of the Experimental Parameters on the Growth of MoS_2 Flakes. *CrystEngComm* **2018**, *20*, 4823−4830.

https://doi.org/10.1021/acs.cgd.3c01369
Cryst. Growth Des. 2024, 24, 2755−2763